Geophysical Research Letters

RESEARCH LETTER
10.1029/2019GL086142

Deformation of the Baige Landslide, Tibet, China, Revealed Through the Integration of Cross-Platform ALOS/PALSAR-1 and ALOS/PALSAR-2 SAR Observations

Xiaojie Liu[1], Chaoying Zhao[1,2], Qin Zhang[1,2], Zhong Lu[3], and Zhenhong Li[1,4]

[1]School of Geological Engineering and Geomatics, Chang'an University, Xi'an, China, [2]State Key Laboratory of Geo-Information Engineering, Xi'an, China, [3]Roy M. Huffington Department of Earth Sciences, Southern Methodist University, Dallas, TX, USA, [4]School of Engineering, Newcastle University, Newcastle, UK

Abstract Twenty-eight ALOS/PALSAR-1 and ALOS/PALSAR-2 images acquired from January 2007 to August 2018 were exploited to characterize the deformation history and temporal evolution of the Baige landslide, China, which successively occurred on 11 October and 3 November 2018. To mitigate the errors caused by the topographic relief and to conduct offset estimates between the SAR images from different platforms, a novel offset-tracking method is proposed. The SAR images were ortho-rectified firstly. Then two-dimensional deformations were retrieved successfully from SAR images acquired at an identical platform and different platforms. Our results indicate that the maximum cumulative deformation in the line-of-sight direction of the Baige landslide reached about −60 m between January 2007 and August 2018. Furthermore, correlation between time series deformation and monthly precipitation and soil moisture derived from SAR intensity images suggests that the failure of the Baige landslide was closely related to the heavy rainfall in the summer of 2018.

Key Points:
- An improved time series SAR offset-tracking chain is proposed to extract the long-term and large gradient landslide motion
- For the first time accurate pixel offsets between cross-platform SAR data sets are achieved
- The cumulative deformation of <−60 m and temporal evolution over 11 years are successfully retrieved at the Baige landslide

Supporting Information:
- Supporting Information S1

Correspondence to:
C. Zhao,
zhaochaoying@163.com

Citation:
Liu, X., Zhao, C., Zhang, Q., Lu, Z., & Li, Z. (2020). Deformation of the Baige landslide, Tibet, China, revealed through the integration of cross-platform ALOS/PALSAR-1 and ALOS/PALSAR-2 SAR observations. *Geophysical Research Letters*, *47*, e2019GL086142. https://doi.org/10.1029/2019GL086142

Received 11 NOV 2019
Accepted 14 JAN 2020
Accepted article online 21 JAN 2020

1. Introduction

The Jinsha River, as the upper reaches of the Yangtze River, flows through four provinces including Qinghai, Tibet, Sichuan, and Yunnan in western China. On 11 October 2018, a high-speed bedrock landslide occurred on the left bank of Jinsha River near Baige village, Jiangda County in the eastern Tibet, China (Fan et al., 2019). The failed material of approximate 24×10^6 m^3 rushed into Jinsha River and formed a barrier lake, which started draining naturally one day later. Unfortunately, on 3 November, the unstable mass of the first landslide collapsed again, producing another volume of 9.13×10^6 m^3 (Ouyang et al., 2019). A new barrier lake with a storage capacity of more than 500×10^6 m^3 was formed, and blocked the Jinsha River once again. These two landslide events have seriously threatened the safety of people's lives and properties on both sides of the Jinsha River and raised widespread concern in society. A total of 67,449 inhabitants were affected and relocated after the occurrence of the Baige landslide (Liang et al., 2019).

It is of great significance to investigate the preevent deformation and its evolution and to capture any possible precursory signals for the prevention and management of landslide disasters. SAR interferometry has proved to be able to retrieve the preevent deformation and determine the acceleration stage prior to the runout. For instance, Kang et al. (2019) detected the acceleration date of the deformation for the 24 June 2017 Maoxian landslide in Sichuan province of China using C-band Sentinel-1 SAR images. Zhao et al. (2019) identified the deformation acceleration dates before the occurrence of two slopes in Heifangtai loess terrace, Gansu province of China using Sentinel-1 SAR images, which were well verified by in-situ measurements. Currently, two main categories of SAR techniques, that is, the phase-based SAR interferometry and the amplitude-based offset-tracking, are well applied in the investigation of landslide for different purposes, including potential landslide detection and mapping over a wide region (Liu et al., 2018), landslide monitoring and modeling (Carlà et al., 2016), landslide mechanism analysis (Zhao et al., 2018), and landslide hazard and risk assessment (Lu et al., 2014).

Phase-based SAR interferometry methods including conventional differential interferometric SAR and multiple aperture interferometry, have the potential to measure deformation with centimeter or subcentimeter precision. However, the prerequisite of these methods is the high coherence between different SAR acquisitions, which makes it a challenge to map landslides in mountain areas with dense vegetation. Moreover, it is

difficult to monitor large gradient deformation due to the saturation of phase fringes and the associated coherence loess (Li et al., 2019). On the other hand, amplitude-based SAR offset-tracking technique can potentially detect and monitor large-gradient deformation, which estimates the azimuth and range offsets using a cross-correlation technique between two amplitude images (Rott et al., 1998). This method has been successfully applied to investigate mining-induced collapse (Yang et al., 2018), volcano eruption (Schaefer et al., 2019), coseismic deformation (Vajedian et al., 2018), and landslide movements (Darvishi et al., 2018; Singleton et al., 2014).

Previous studies showed that the preevent deformation rate of the Baige landslide reached several meters per year (Fan et al., 2019; Ouyang et al., 2019), which makes it impossible to monitor the movement of the landslide using the phase-based SAR interferometry. On the other hand, mapping the landslide motion using the amplitude-based method requires the removal of artifacts caused by great topographic relief for the long perpendicular baseline pairs. Furthermore, the offset estimates between the SAR images from different platforms have not been attempted, which potentially can provide uninterrupted time series deformation for landslide monitoring.

In this study, an improved time series offset-tracking method is presented. Firstly, the pixel misalignments in SAR images caused by topographic relief and incidence angle difference are effectively eliminated using an ortho-rectification method. Secondly, the preevent time series deformation of the Baige landslide in the past 11 years are successfully retrieved using SAR images that are not interferometrically compatible. Lastly, the evolution stages and triggering factors of the Baige landslide are analyzed.

2. Study Area and Data Sets

2.1. Geological Settings

The Baige landslide indicated by the red rectangle in Figure S1a is located at the junction of Baiyu county of Sichuan province and Jiangda county of Tibet (Ouyang et al., 2019). It belongs to the freeze-thaw plateau area in southern Sichuan and Tibet, with a temperature and annual precipitation of about 8.0 °C and 627 mm/year, respectively (Fan et al., 2019). The elevation of the study area is more than 3,000 m in general, and even more than 4,500 m in some local area (Figure S1a). The height difference from the top to the bottom of the landslide is about 828 m, formed the slopes ranging from 35° to 55°. The geological setting of the study area is conditioned by several NW trending faults and folds (Figure S1b). The strata outcropping in the study area includes Xiongsong (Xi_2), Shengpa (Sh), Xianisongduo (Xi_1), and Jingu (Ji) formations of Upper Carboniferous, Upper Triassic, and Upper Ordovician periods (Figure S1b). They mainly composed of limestone (T_3jn), gneiss (P_txn^a), serpentinite ($\phi_{\omega 4}$), and granite ($\gamma\delta_5^2$). The landslide is located at the edge of the Boluo-Muxie fault (Figure S1b), formed a band of crushed rock composed of gneiss and serpentinite with a width of about 300 m, which makes it prone to sliding (Fan et al., 2019).

2.2. Data Sets

In order to quantitatively monitor the long-term time series deformation of the Baige landslide, a total of 28 SAR images acquired by L-band ALOS/PALSAR-1 and ALOS/PALSAR-2 satellites from January 2007 to March 2011 and from October 2014 to August 2018 were collected. The basic parameters of the SAR data are presented in Table S1, while their spatial coverages are shown in Figure S1a. Besides, an external digital elevation model with a spatial resolution of 30 m, generated from the Shuttle Radar Topography Mission, was used to assist in ortho-rectification of the SAR images.

In order to make full use of SAR images available and to reduce the error propagation, a new offset pair combination strategy is proposed. That is, we only set the lower bound of temporal baseline regardless of the perpendicular baseline. In this study, the lower bounds of temporal baseline for ALOS/PALSAR-1 and ALOS/PALSAR-2 SAR data sets were 300 and 70 days, respectively, with the consideration of surface deformation velocity. To bridge the gap between ALOS/PALSAR-1 and ALOS/PALSAR-2 SAR data sets, three adjacent images for each platform were chosen to shorten the temporal baseline and give certain redundancy. Finally, a total of 83 offset pairs were kept in this study, including 31 ALOS/PALSAR-1 pairs, 44 ALOS/PALSAR-2 pairs, and 8 pairs between ALOS/PALSAR-1 and ALOS/PALSAR-2 images. The spatial-temporal baseline distributions of the selected offset pairs are shown in Figure S2.

3. Methodology

In order to retrieve the preevent deformation and the temporal evolution of the Baige landslide, an improved SAR amplitude offset-tracking method is proposed (Figure S3), which can estimate the two-dimensional (2-D) offsets between SAR images not only from an identical platform (e.g., ALOS/PALSAR-1 and ALOS/PALSAR-1 images or ALOS/PALSAR-2 and ALOS/PALSAR-2 images) but also from different platforms (e.g., ALOS/PALSAR-1 and ALOS/PALSAR-2 images). Firstly, for the SAR images from an identical platform, the master images within ALOS/PALSAR-1 and ALOS/PALSAR-2 data sets were determined, respectively, by considering the temporal baseline, perpendicular baseline, and Doppler central frequency variations. To link the SAR images from ALOS/PALSAR-1 and ALOS/PALSAR-2 SAR satellites, the master image of ALOS/PALSAR-2 SAR data was set arbitrarily as the final master image. Secondly, all the slave images were ortho-rectified and co-registered with respect to their corresponding master image. Thirdly, the offset pairs were generated by setting the lower bounds of temporal baseline for SAR data sets regardless of the perpendicular baseline. Fourthly, 2-D offsets in line-of-sight (LOS) and azimuth directions of all offset pairs were calculated using the pixel offset-tracking method (Strozzi et al., 2002). Finally, 2-D deformation results of each offset pair were geocoded into the given geographic coordinate system, and combined to invert 2-D deformation rate and time series using singular value decomposition.

The procedure of SAR images ortho-rectification is shown as follows (Chen, 2004; Li et al., 2014; Lu & Dzurisin, 2010; Werner et al., 2000):

i An external digital elevation model is accurately co-registered to the master image. The initial transformation relationship between the master and slave images is built according to their imaging geometries based on the Range-Doppler equations (Curlander, 1982).
ii The initial transformation relationship might contain errors due to the uncertainties in the digital elevation model and the orbital state vectors, and hence, it needs to be improved. The improvement is based on the resampling of the master SAR intensity image to the geometry of the slave intensity image, then the offsets between the two images are estimated and then used to improve the initial transformation relationship.
iii The rectified SAR image is obtained by resampling the slave SAR images to the master SAR image geometry using the improved transformation relationship. The offset estimation is conducted again to remove some residual offsets to obtain the accurately rectified SAR images.

As for the rectified SAR images, the pixel misalignments caused by topographic relief and incidence angle difference are effectively eliminated, which can be employed for offset estimation. Amplitude cross-correlation method was used to estimate the offsets; at each pixel location, a varying window size of 64 to 128 pixels rather than a fixed window was employed to avoid the discontinuous offsets to some extent (Zhao et al., 2013). At each location, the offset estimation with the highest signal-to-noise ratio was retained as the final results. As the topographic relief and incidence angle difference effects have been rectified before, the 2-D offsets can be directly transferred into the 2-D deformation of the landslide.

4. Results and Analyses

4.1. The 2-D Deformation Retrieved From Cross-Platform SAR Images

In order to reveal the deformation characteristics and temporal evolution of the Baige landslide in the past 11 years, we conducted offset estimation between the ALOS/PALSAR-1 and ALOS/PALSAR-2 images. For the traditional offset-tracking methods (Casu et al., 2011; Li et al., 2019; Sun et al., 2017), the strategies of small spatial and temporal baselines and/or small spatial baselines and large temporal baselines are used to generate offset pairs. Then, the SAR images are initially co-registered based on the amplitude information, and the initial offsets between two images are estimated using precise orbit information. Next, the precise co-registration is conducted for the given patch number (e.g., 100 by 100) with a certain window size (e.g., 256 by 256). The two-dimensional offsets for each patch are estimated with the normalized cross-correlation method between two amplitude images (Sun et al., 2017). Finally, the offset tracking is conducted by estimating two-dimensional offsets for each pixel with normalized cross-correlation method, where pixels with normalized cross-correlation coefficients and signal-to-noise ratio values larger than a given threshold are accepted. Figure 1 shows 2-D deformation results between an ALOS/PALSAR-1 and ALOS/PALSAR-2

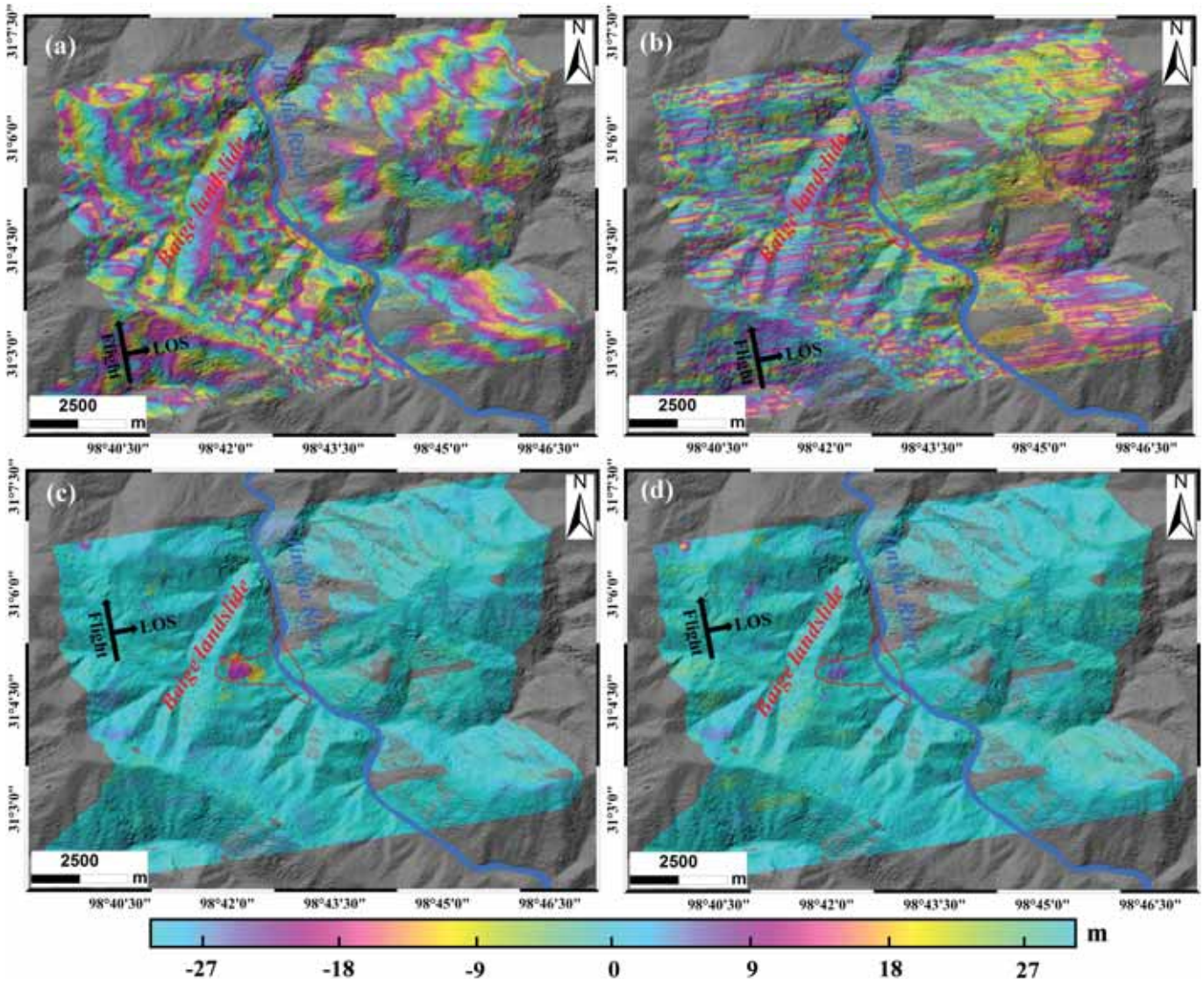

Figure 1. Two-dimensional deformation maps between ALOS/PALSAR-1 image acquired on 25 February 2010 and ALOS/PALSAR-2 image acquired on 27 July 2015 derived by the traditional and the improved offset-tracking methods. (a) LOS deformation derived by the traditional method. (b) Azimuth deformation derived by the traditional method. (c) LOS deformation derived by the improved method. (d) Azimuth deformation derived by the improved method.

pair calculated with the traditional (Figures 1a and 1b) and the improved (Figures 1c and 1d) offset-tracking methods, respectively, where the temporal and perpendicular baselines are 1,978 days and 27,972 m, respectively. The original and the ortho-rectified intensity images of the ALOS/PALSAR-1 and ALOS/PALSAR-2 pair are presented in Figure S5. It can be seen from Figures 1a and 1b that 2-D deformation fields of the landslide are completely contaminated by the artifacts resulted from the great topographic relief and incidence angle difference. Owing to the ortho-rectification of SAR images before SAR co-registration, 2-D deformation fields shown in Figures 1c and 1d are successfully retrieved, where the maximum cumulative deformation of the landslide in the LOS and azimuth directions reached −22 and 6 m from 25 February 2010 to 27 July 2015, respectively.

4.2. Long-Term Preevent Deformation of the Baige Landslide

The preevent deformation rate and time series of the Baige landslide from January 2007 to August 2018 are retrieved using the improved offset-tracking method. The annual deformation rates in both LOS and azimuth directions are shown in Figure 2, where Figures 2a and 2b are the LOS and azimuth deformation

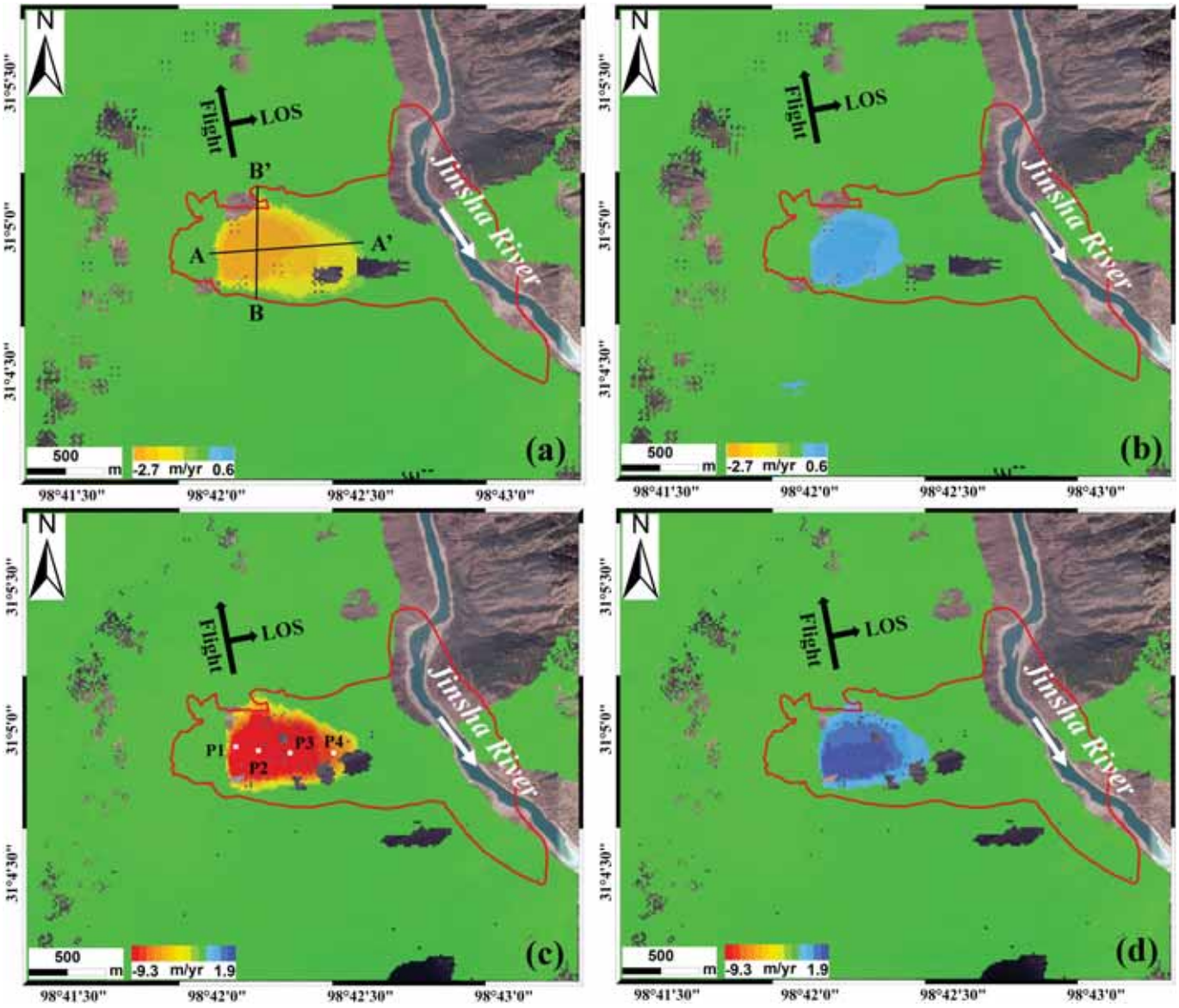

Figure 2. Preevent deformation rate maps of the Baige landslide. The red solid lines indicate the boundary of the landslide. (a) Deformation rate map in the LOS direction retrieved by ALOS/PALSAR-1 images from January 2007 to March 2011. (b) Deformation rate map in the azimuth direction retrieved by ALOS/PALSAR-1 images from January 2007 to March 2011. (c) Deformation rate map in the LOS direction retrieved by ALOS/PALSAR-2 images from October 2014 to August 2018. (d) Deformation rate map in the azimuth direction retrieved by ALOS/PALSAR-2 images from October 2014 to August 2018.

rates calculated with ALOS/PALSAR-1 images from January 2007 to March 2011, respectively, and Figures 2c and 2d are the deformation rates calculated with ALOS/PALSAR-2 images from October 2014 to August 2018, respectively. Note that negative values in Figures 2a and 2c indicate that the landslide are moving away from the sensors, and positive values in Figures 2b and 2d represent the movement opposite to the flight direction. It can be seen from Figure 2 that the boundary of unstable landslide is clearly depicted by the deformation rate maps. It is evident that the landslide not only has the vertical and east-west deformation components (see Figures 2a and 2c) but also has a north-south deformation (see Figures 2b and 2d). The deformation rates in the LOS and azimuth directions from January 2007 to March 2011 reached −2.7 and 0.6 m/year, respectively, which increased to −9.3 and 1.9 m/year from October 2014 to August 2018, respectively. In addition, it can be inferred from Figures 1c and 1d that the deformation rates in the LOS and azimuth directions were −4.3 and 1.2 m/year from February 2010 to

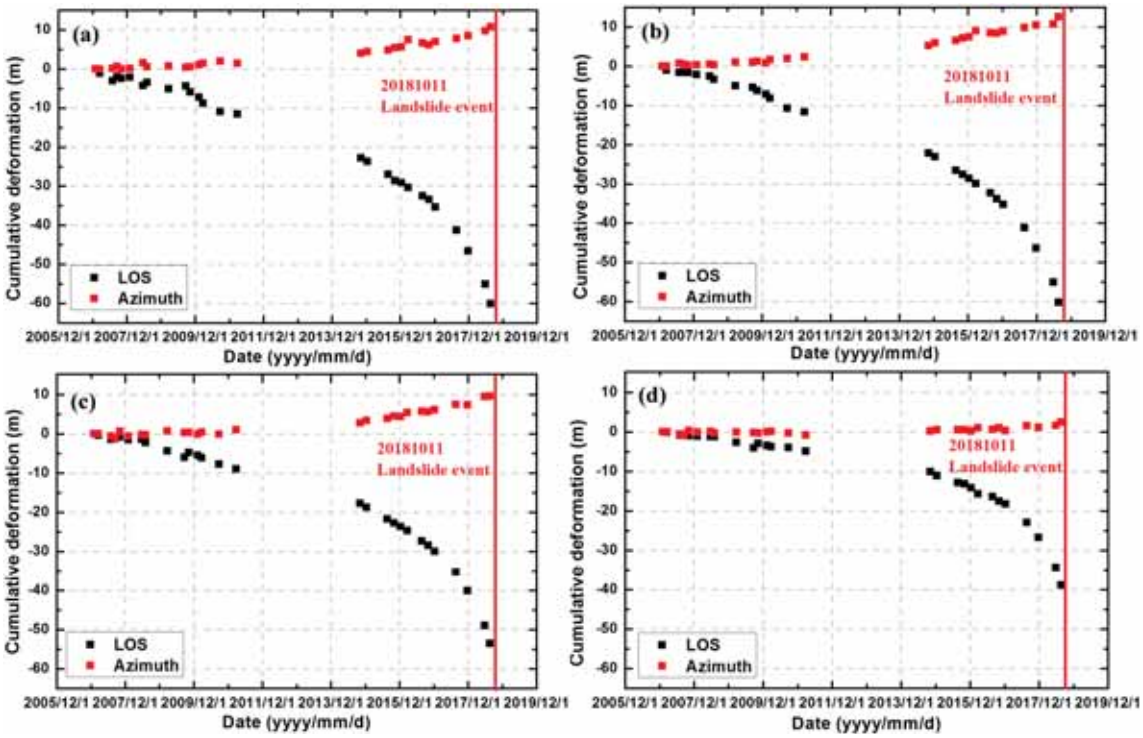

Figure 3. Two-dimensional time series deformations of the Baige landslide for Points (a) P1, (b) P2, (c) P3, and (d) P4 from January 2007 to August 2018. The locations of Points P1–P4 are marked in Figure 2c with white solid rectangles.

July 2015, respectively. That is, the deformation of the Baige landslide increased continuously in three directions, and the landslide is dominated by the vertical and east-west deformation.

Four feature points located at the different areas of the landslide were selected to analyze the temporal deformation history. Two-dimensional time series deformations of four selected points from January 2007 to August 2018 are shown in Figure 3. The maximum cumulative deformation was observed at P2 (the middle part of the landslide), and the cumulative deformations in the LOS and azimuth directions reached −60.2 and 12.6 m, respectively. The minimum cumulative deformation occurred at P4 (the lower part of the landslide), and the cumulative deformations in the LOS and azimuth directions were −38.8 and 2.5 m, respectively. The nonlinear deformation trend was observed at all four points from January 2007 to August 2018. After 27 July 2015, an obvious acceleration trend was observed, which will be analyzed and discussed in detail in section 5.1.

5. Discussion

5.1. Deformation Stages of the Baige Landslide

According to the theory of creep deformation (Saito, 1969), the approaching failures of landslides usually experience three consecutive stages (Figure S7a), that is, initial deformation stage (primary creep), constant deformation stage (secondary creep), and accelerative deformation stage. We redraw the time series deformation curve of Point P2 in Figure 2c as shown in Figure S7b. It can be seen that the deformation evolution of the Baige landslide obeys the creep deformation theory. Accordingly, we can infer that the landslide suffered the initial deformation stage before 10 January 2010 with the deformation rate of 6 mm/day. Unfortunately, no appropriate SAR images could be used before January 2007. Subsequently, the landslide entered the constant deformation stage with the deformation rate of 10 mm/day, and finally, it turned to the accelerative deformation stage on 27 July 2015. During the last stage, we can also roughly subdivide it into three stages, that is, initial acceleration stage from 27 July 2015 to 3 October 2016 with the deformation rate of 17 mm/day, medium-term acceleration stage with the deformation rate of 35 mm/day, and sliding stage after 28 May 2018 with the deformation rate as large as 92 mm/day. Eventually, the landslide occurred on

11 October 2018. It would be possible to make an early warning of the landslide if such an acceleration process was captured in advance.

5.2. Triggering Factors of the Baige Landslide

The landslide deformation is typically determined by internal geological conditions and external triggering factors such as seasonal precipitation, reservoir water-level fluctuations, tectonic movement, agricultural irrigation, and deforestation among others (Li et al., 2019; Liu et al., 2018; Singleton et al., 2014; Sun et al., 2017; Zhao et al., 2018). Heavy rainfall can trigger the slope failure and influence the mobility and eventual runout of the landslide by increasing the basal pore water pressure. As one of the key factors to understanding the landslide events at regional and global scales, the increase of soil moisture after precipitation often reduce the stability of landslide by decreasing frictional resistance and the strength of materials. The soil moisture can be depicted using the proximity of SAR intensity backscattering coefficient (Zhao et al., 2018); that is, the radar backscattering coefficients increase with soil moisture. Accordingly, the changes in the backscattering coefficients of SAR intensity can reflect the changes in soil moisture. In order to analyze the triggering factors of the Baige landslide, we conduct a correlation analysis between the deformation rate, time series deformation, soil moisture derived from SAR intensity images, and monthly precipitation, as shown in Figure S8, where some conclusions can be drawn as follows:

i The precipitation in the study area is mainly concentrated in summer, from June to September. In the past 11 years, the maximum precipitation took place in August 2018. The high correlation between the landslide deformation rate and the monthly precipitation can be clearly seen. However, the deformation acceleration lagged the precipitation around one to two months. It is difficult to determine the exact lag time due to the low temporal sampling and uneven SAR acquisitions.

ii The backscattering coefficients of SAR intensity image are closely correlated with the precipitation, and the backscattering coefficients in dry seasons are obviously lower than those in rainy seasons, which suggests that the radar backscattering can reflect the soil moisture changes to a certain extent. We can see that there is also a certain correlation between the deformation rate and the soil moisture.

iii It can be concluded that the failure of the Baige landslide was jointly affected by internal geological conditions and external triggering factors (i.e., heavy precipitation in summer and the increase in soil moisture). The landslide is located at the band of crushed rock composed of gneiss and serpentinite, which makes it prone to sliding. The heavy precipitation in August 2018 decreased the frictional resistance and the strength of materials, eventually led to the failure.

6. Conclusions

To overcome the effects of topographic relief on the offset-tracking derived deformation measurements, especially from cross-platform SAR images, an improved offset-tracking method has been demonstrated. This new method enables us to derive large gradient deformation from cross-platform SAR observations and recover historic deformation. Then, the preevent deformation characteristics and temporal evolution of the Baige landslide was investigated by using the improved method. The results illustrate that the Baige landslide exhibited dramatic deformation from January 2007 to August 2018 with the maximum cumulative deformation of about −60 m in the LOS direction. The temporal evolution of the landslide deformation is highly consistent with the standard creep curve of landsides. Specifically, the time node of the landslide deformation acceleration was clearly captured by integrating long-term ALOS/PALSAR-1 and ALOS/PALSAR-2 images. Such promising results suggest that SAR technique can be applied for long-term and midterm landslide warning, which can provide practical guideline to the field measurement. In addition, the correlation analysis between monthly precipitation and landslide deformation revealed the triggering factor of this landslide, which provides an important reference for the prevention and management of landslide disasters in other areas of Jinsha River catchment.

Acknowledgments
This research is funded by the Natural Science Foundation of China (grants 41731066, 41874005, 41929001), the Fundamental Research Funds for the Central University (grants 300102269303, 300102269712, 300102269104), and the 111 project (B18046). ALOS/PALSAR-1 and ALOS/PALSAR-2 images were provided by the Japan Aerospace Exploration Agency (JAXA) under grant P3222002 for the purpose of scientific research and can be found from https://auig2.jaxa.jp/ips/home?language=en_US. Ownership and copyright of ALOS/PALSAR-1 and ALOS/PALSAR-2 images belong to JAXA. One arc-second SRTM DEM was publicly available through the website http://e4ftl01.cr.usgs.gov/MODV6_Dal_D/SRTM/SRTMGL1.003/2000.02.11/. Precipitation data were publicly available from the website https://pmm.nasa.gov/data-access/downloads/gpm. Several figures were prepared by using ArcGIS, Origin, and Python software. We also thank two anonymous reviewers as well as the Editor for their insightful comments and suggestions.

References

Carlà, T., Raspini, F., Intrieri, E., & Casagli, N. (2016). A simple method to help determine landslide susceptibility from spaceborne InSAR data: The Montescaglioso case study. *Environmental Earth Sciences*, *75*(24), 1–12. https://doi.org/10.1007/s12665-016-6308-8

Casu, F., Manconi, A., Pepe, A., & Lanari, R. (2011). Deformation time-series generation in areas characterized by large displacement dynamics: The SAR amplitude pixel-offset SBAS technique. *IEEE Transactions on Geoscience and Remote Sensing*, *49*(7), 2752–2763. https://doi.org/10.1109/TGRS.2010.2104325

Chen, E. (2004). Study on ortho-rectification methodology of space-borne synthetic aperture radar image, (Doctoral Dissertation). Retrieved from CNKI. (http://www.cnki.net/). Beijing: Chinese Academy of Forestry. (In Chinese)

Curlander, J. (1982). Location of space-borne SAR imagery. *IEEE Transactions on Geoscience and Remote Sensing*, *20*(3), 359–364. https://doi.org/, https://doi.org/10.1109/TGRS.1982.350455

Darvishi, M., Schlögel, R., Bruzzone, L., & Guozzo, G. (2018). Integration of PSI, MAI, and intensity-based sub-pixel offset tracking results for landslide monitoring with X-band corner reflectors—Italian Alps (Corvara). *Remote Sensing*, *2018*(10), 409. https://doi.org/10.3390/rs10030409

Fan, X., Xu, Q., Alonso-Rodriguez, A., Subramanian, S., Li, W., Zheng, G., et al. (2019). Successive landsliding and damming of the Jinsha River in eastern Tibet, China: Prime investigation, early warning, and emergency response. *Landslides*, *16*, 1059. https://doi.org/10.1007/s10346-019-01165-z

Kang, Y., Lu, Z., Zhao, C., Zhang, Q., Kim, J., & Niu, Y. (2019). Diagnosis of Xinmo (China) landslide based on interferometric synthetic aperture radar observation and modeling. *Remote Sensing*, *11*, 1846. https://doi.org/10.3390/rs11161846

Li, J., Li, Z., Ding, X., Wang, Q., Zhu, J., & Wang, C. (2014). Investigating mountain glacier motion with the method of SAR intensity-tracking: Removal of topographic effects and analysis of the dynamic patterns. *Earth-Science Reviews*, *138*, 179–185. https://doi.org/10.1016/j.earscirev.2014.08.016

Li, M., Zhang, L., Shi, X., Liao, M., & Yang, M. (2019). Monitoring active motion of the Guobu landslide near the Laxiwa Hydropower Station in China by time-series point-like targets offset tracking. *Remote Sensing of Environment*, *221*, 80–93. https://doi.org/10.1016/j.rse.2018.11.006

Liang, G., Wang, Z., Zhang, G., & Wu, L. (2019). Two huge landslides that took place in quick succession within a month at the same location of Jinsha River. *Landslides*, *16*, 1059–1062. https://doi.org/10.1007/s10346-019-01165-z

Liu, X., Zhao, C., Zhang, Q., Peng, J., Zhu, W., & Lu, Z. (2018). Multi-temporal loess landslide inventory mapping with C-, X- and L-band SAR datasets—A case study of Heifangtai loess landslides, China. *Remote Sensing*, *2018*, 10(11). https://doi.org/10.3390/rs10111756

Lu, P., Casagli, N., Tofani, V., & Catani, F. (2014). Quantitative hazard and risk assessment for slow-moving landslides from persistent scatterer interferometry. *Landslides*, *11*(4), 685–696. https://doi.org/10.1007/s10346-013-0432-2

Lu, Z., & Dzurisin, D. (2010). Ground surface deformation patterns, magma supply, and magma storage at Okmok volcano, Alaska, from InSAR analysis: 2. Coeruptive deflation, July–August 2008. *Journal of Geophysical Research*, *115*, B00B03. https://doi.org/101029/2009JB006970

Ouyang, C., An, H., Zhou, S., Wang, Z., Su, P., Wang, D., et al. (2019). Insights from the failure and dynamic characteristics of two sequential landslides at Baige village along the Jinsha River. *China. Landslides*, 1–18. https://doi.org/10.1007/s10346-019-01177-9

Rott, H., Stuefer, M., Siegel, A., Skvarca, P., & Eckstaller, A. (1998). Mass fluxes and dynamics of Moreno Glacier, Southern Patagonia Icefield. *Geophysical Research Letters*, *25*(9), 1407–1410. https://doi.org/10.1029/98GL00833

Saito, M. (1969). Forecasting time of slope failure by tertiary creep. Paper presented at Proceedings of 7th international conference on soil mechanics and foundation engineering, 677-683.

Schaefer, L., Traglia, F., Chaussard, E., Lu, Z., Nolesini, T., & Casagli, N. (2019). Monitoring volcano slope instability with Synthetic Aperture Radar: A review and new data from Pacaya (Guatemala) and Stromboli (Italy) volcanoes. *Earth-Science Reviews*, *192*, 236–257. https://doi.org/10.1016/j.earscirev.2019.03.009

Singleton, A., Li, Z., Hoey, T., & Muller, J. (2014). Evaluating sub-pixel offset techniques as an alternative to D-InSAR for monitoring episodic landslide movements in vegetated terrain. *Remote Sensing of Environment*, *147*, 133–144. https://doi.org/10.1016/j.rse.2014.03.003

Strozzi, T., Luckman, A., Murray, T., Wegmülller, U., & Werner, C. L. (2002). Glacier motion estimation using SAR offset-tracking procedures. *IEEE Transactions on Geoscience and Remote Sensing*, *40*(11), 2384–2391. https://doi.org/10.1109/TGRS.2002.805079

Sun, L., Muller, J., & Chen, J. (2017). Time series analysis of very slow landslides in the Three Gorges region through small baseline SAR offset tracking. *Remote Sensing*, *9*, 1314. https://doi.org/10.3390/rs9121314

Vajedian, S., Motagh, M., Mousavi, Z., Motaghi, K., Fielding, E., Akbari, B., et al. (2018). Coseismic deformation field of the M_w 7.3 12 November 2017 Sarpol-e Zahab (Iran) earthquake: A decoupling horizon in the northern Zagros Mountains inferred from InSAR observations. *Remote Sensing*, *10*, 1589. https://doi.org/10.3390/rs10101589

Werner, C., Wegmüller, U., Strozzi, T., & Wiesmann, A. (2000). *GAMMA SAR and interferometric processing software*. Paper presented at Proceedings of the ERS-Envisat Symposium. Sweden: Gothenburg.

Yang, Z., Li, Z., Zhu, J., Preusse, A., Hu, J., Feng, G., & Papst, M. (2018). Time-series 3-D mining-induced large displacement modeling and robust estimation from a single-geometry SAR amplitude data set. *IEEE Transactions on Geoscience and Remote Sensing*, *6*, 3600-3610. https://dx.doi.org/https://doi.org/10.1109/TGRS.2018.2802919

Zhao, C., Kang, Y., Zhang, Q., Lu, Z., & Li, B. (2018). Landslide identification and monitoring along the Jinsha River catchment (Wudongde reservoir area), China, using the InSAR method. *Remote Sensing*, *10*, 993. https://doi.org/10.3390/rs10070993

Zhao, C., Liu, X., Zhang, Q., Peng, J., & Xu, Q. (2019). Research on loess landslide identification, monitoring and failure mode with InSAR technique in Heifangtai, Gansu. *Geomatics and Information Science of Wuhan University*, *7*(44), 996–1007. (In Chinese). https://doi.org/10.13203/j.whugis20190072

Zhao, C., Lu, Z., & Zhang, Q. (2013). Time series deformation monitoring over mining regions with SAR intensity-based offset measurements. *Remote Sensing Letters, 2013*, *5*(4), 436–445. https://doi.org/10.1080/2150704X.2012.746482

References From the Supporting Information

Berardino, P., Fornaro, G., Lanari, R., & Sansosti, E. (2002). A new algorithm for surface deformation monitoring based on small baseline differential SAR interferograms. *IEEE Transactions on Geoscience and Remote Sensing*, *40*, 2375–2383. https://doi.org/10.1109/TGRS.2002.803792

Sansosti, E., Berardino, P., Manunta, M., Serafino, F., & Fornaro, G. (2006). Geometrical SAR image registration. *IEEE Transactions on Geoscience and Remote Sensing*, *44*(10), 2861–2870. https://doi.org/10.1109/TGRS.2006.875787